

Probing the strongly correlated magnetic state of Co₂C nanoparticles at low temperatures using μ SR

Nirmal Roy¹, P C Mahato¹, Suprotim Saha¹, M. Telling², J. S. Lord², D T Adroja^{2,3}, S. S. Banerjee^{1,+}

¹*Indian Institute of Technology Kanpur, Kanpur, Uttar Pradesh 208016, India*

²*ISIS Facility, Rutherford Appleton Laboratory, Chilton, Didcot Oxon OX11 0QX, United Kingdom*

³*Highly Correlated Matter Research Group, Physics Department, University of Johannesburg, P.O. Box 524, Auckland Park 2006, South Africa*

Abstract:

Co₂C nanoparticles (NPs) are amongst transition metal carbides whose magnetic properties have not been well explored. A recent study by Nirmal Roy et al. [1] showed that a collection of Co₂C NPs exhibit exchange bias (EB) effect below $T_{EB} = 50$ K and also a spin glass (SG) state below $T_{SG} = 5$ K. We use magnetic, electrical transport, specific heat, and muon spin rotation (μ SR) measurements to explore further the magnetic properties of a pellet made with 40 nm diameter pure Co₂C NPs. We uncover the onset of Kondo localization at Kondo temperature $T_K (= 40.1$ K), which is close to the onset temperature (T_{EB}) of the EB effect. A crossover from the Kondo-screened scenario to an RKKY interaction-dominated regime is also observed for $T < T_K$. Temperature-dependent specific heat measurement further supports the Kondo localization scenario in the pellet and shows the heavy fermionic nature of the strongly correlated electronic state in Co₂C. The zero field μ SR asymmetry spectra in the low-temperature regime are characterized by two distinct fast and slow relaxation rates. The spectra show the absence of long-range magnetic order in the sample. However, our analysis suggests the NPs-pellet shows the presence of a dominant magnetically disordered fraction and a smaller fraction with short-range order. Muons in the disordered fraction exhibit a slower relaxation rate, while muons in the smaller fraction with short-range order exhibit a faster relaxation rate. We observe an increase in this fast relaxation rate between T_{EB} and T_{SG} . This increase below $T_{EB} \sim 50$ K suggests a slowing down of the fluctuating local magnetic environment around muons. Transverse field (TF) - μ SR asymmetry spectra show the emergence of a stable, multi-peaked local magnetic field distribution in the pellet below T_{EB} . Longitudinal field (LF) μ SR spectra shows distinct changes in the dynamics of fluctuations suggesting the presence of a frozen glassy like state below 6 K. Based on our results, we suggest that below T_{EB} , the pellet of Co₂C NPs develops a magnetic interface that separates the two magnetic fractions; one is a

disordered fraction, and the other is a fraction with short-range order. The exchange interaction that sets in below T_{EB} at the interface couples the two fractions, leading to a suppression of the fluctuations. With the suppression of magnetic fluctuations below T_{EB} , strong correlation effects in the electronic state of Co_2C lead to Kondo localization.

I. INTRODUCTION:

In the core-shell nanoparticles (NPs) system, a wide variety of complex effects and phases like the exchange bias (EB) effect, spin glass (SG) phase, spin-liquid phases, the spin ice phase, magnetic proximity effect [2-8], have been reported. The manipulation of core and shell dimensions and exploring different materials produce unique properties in these core-shell [4, 9, 10] NPs. The EB effect relates to two different magnetic species exchange-coupled across an interface. In general, for a ferromagnet (FM) – antiferromagnet (AFM) heterostructure, the system is cooled from above the AFM Néel temperature (T_N) to below it by applying a magnetic field that can saturate the FM. The AFM lattice spins in its ordered state via interfacial exchange coupling to the FM spins pins the latter in a preferred direction creating an additional unidirectional anisotropy. This EB interfacial exchange anisotropy results in an asymmetric shift of the magnetization (M) vs. the applied field (H) hysteresis loops along the field and magnetization axis compared to the typical symmetric loop found in a simple bulk FM. The EB effect is significant for spintronic devices and magnetic information storage technology [11-13]. Therefore, the EB effect continues to be a popular investigated phenomenon studied in core-shell NPs. It was first discovered in the FM cobalt (Co)/AFM cobalt oxide (CoO) system [14]. Since then, EB has been reported in a plethora of systems consisting of clusters of small particles, FM films deposited on a single crystal or polycrystalline AFMs, FM/AFM thin-film bilayers, FM/ferrimagnet, FM/spin-glass heterostructures [15-19]. The fascinating magnetic properties of these NP systems originate from the complex interplay of finite size and surface effects, making them very different from their bulk counterpart [20]. In some magnetic NPs, although the core may be magnetically ordered, there can be local symmetry breaking near the surface of the NPs, producing a magnetically disordered spin configuration structure.

In these NPs, a magnetic core-shell structure naturally emerges with a magnetically ordered core and a disordered spin configuration on the shell. An exchange coupling at the interface between this disordered shell and the ordered core gives rise to EB in these systems [10].

In recent times, bulk magnetization studies of Cobalt Carbide (Co_2C) NPs have unraveled some intriguing features of its magnetism at nanoscales. Among the well-known transition metal carbides (TMC), the magnetic properties of Co_2C have not been well explored [21, 22]. TMCs are well known for their extreme hardness, high thermal and electrical conduction, high coercive fields (H_c), and high magnetic anisotropy [21-25]. The high magnetic anisotropy makes these TMCs suitable candidates for application as rare-earth-free permanent magnets and as magnetic storage devices if their magnetic properties can be tailored and controlled at the nanoscale [26]. While DFT calculations suggest Co_2C is a paramagnet in the bulk form [27], early studies showed that NPs of Co_2C are ferromagnetic [28, 29]. More recent magnetic measurements [1] show that the ferromagnetism in the sample made from 40 nm diameter Co_2C NPs survives up to room temperature. This result suggested that a high blocking temperature (exceeding 300 K) or large magnetic anisotropy is associated with these NPs. Furthermore, below $T_{EB} = 50$ K, these NPs exhibit a significant EB effect with an exchange bias field ~ 0.25 kOe at 2 K. Studies also showed that the Co_2C NPs sample exhibits a low-temperature SG phase that appears below $T_{SG} \sim 5$ K [1]. Furthermore, DFT investigations [1] suggest the Co_2C may have a structurally ordered core and a structurally disordered shell configuration. These intriguing results suggest a need to probe the local magnetic configuration in the composites made from Co_2C NPs.

Here, using magnetic, electrical transport, thermal and μSR measurements, we explore the internal magnetic properties of a pellet made with 40 nm diameter pure Co_2C NPs. By analysing our resistance (R) versus temperature (T) behaviour we uncover three distinct

regimes for our Co₂C NPs-pellet. The regime III is the high T region > 50 K (which is the exchange bias T , T_{EB}), where transport is governed by electron-phonon interaction mediated scattering. Below T_{EB} , in regime II $R(T)$ behaviour shows Kondo localization and features associated with scattering from these regions. In region I for $T < 35$ K, the transport behaviour fits to system which not only exhibits Kondo localization but there is interaction between localized sites through Ruderman-Kittel-Kasuya-Yosida (RKKY) interactions. The Kondo localization temperature is estimated to be $T_K = 40.1$ K. At T_K , a broad peak is seen in the magnetic contribution to heat capacity. A large value of the Sommerfeld constant (γ) suggests Co₂C is a heavy-fermion system with a strongly correlated electronic state. Zero-field (ZF) μ SR study shows that the asymmetry spectra are characterized by two distinct relaxation rates, indicating two inequivalent stopping sites in the Co₂C NPs-pellet. We see no evidence of long-range magnetic order in the NPs-pellet in our investigation's temperature range of 1.8 K to 220 K. However, the ZF- μ SR spectra analysis suggests the presence of a dominant magnetically disordered fraction with a slower relaxation rate and a smaller fraction with short-range order having a much faster relaxation rate. The rate of the fast-relaxing component is seen to increase between T_{EB} and T_{SG} ; it decreases below T_{SG} . This increase is related to the stabilization of fluctuating magnetic moments below $T_{EB} \sim 50$ K. Concomitant with the onset of stabilization of the fluctuations, analysis of the transverse field μ SR asymmetry spectra (TF- μ SR) shows the emergence of a multi-peaked magnetic field distribution inside the NPs below T_{EB} . Longitudinal field (LF) μ SR spectra shows distinct changes in the dynamics of fluctuations suggesting the presence of a frozen glassy like state below 6 K. Our results suggest that below T_{EB} , a magnetic interface appears, which separates two magnetic fractions. One is the fraction with short-range order, and the other is the magnetically disordered fraction. Below T_{EB} , the exchange interaction at the interface couples the two magnetic fractions and reduces the

fluctuations of the magnetic moments. With the stabilization of fluctuations, the strong correlation effects in Co₂C lead to Kondo localization at magnetic ionic sites below T_{EB} .

II. EXPERIMENTAL RESULTS AND DISCUSSION

Magnetic behavior as a function of T of Co₂C NP pellet:

The method for synthesis of 40 nm diameter Co₂C NP powders and their structural and morphological characterization using powder XRD and TEM are discussed in supplementary information section I (SI-I) and elsewhere [1, 30]. The powders of Co₂C NPs from this batch were compactified into cylindrical pellets with a diameter of 8 mm and thickness of 1 mm, and these pellets were used for magnetic, transport, and thermal measurements. A cylindrical pellet of size 16 mm diameter and thickness 1 mm were also made from the Co₂C NPs for the μ SR measurements. The magnetic measurements were performed in the temperature range of 2 K-300 K using a superconducting quantum interference device (SQUID), Cryogenic UK. Consistent with our earlier results [1], the current pellet of Co₂C NPs from the same batch also shows a robust M - H hysteresis persisting up to 300 K. At low T , particularly below $T_{EB} = 50$ K, the pellet shows the EB effect. Figure 1(a) shows field cooled (FC) hysteresis loops at 2 K and 60 K, wherein a cooling field of 3 T was applied at 300 K before cooling down the sample to the desired T . It is evident from Fig. 1(a) that there is an asymmetry (H_L (left coercive field) $> H_R$ (right coercive field)) in the M - H loop at 2 K, compared to the symmetric M - H loop of 60 K ($> T_{EB}$). Figure 1(b) shows the variation of the exchange bias field $H_{EB} = \frac{|H_L| - |H_R|}{2}$, (H_L and H_R are identified in Fig. 1(a)) with T in a log-linear plot. The blue line is the linear fit that shows the exponential T dependence of $H_{EB}(T)$. An earlier detailed analysis of the training effect established the presence of the EB effect in NPs of Co₂C [1]. AC susceptibility study in Fig. 1(c) also confirms [1] the presence of a broad peak ~ 5 K, which shifts with the excitation frequency (f). This peak represents the SG transition at $T_{SG} \sim 5$ K in the Co₂C NPs-pellet

sample[31]. Our earlier studies using Co₂C NPs made from the same batch have confirmed that this peak in AC susceptibility at 5 K corresponds to an SG transition. It has also been shown that its shift in the peak with frequency obeys the Vogel-Fulcher law, which suggests an SG phase. The SG transition was also confirmed from features seen in DC magnetization studies as well (see Ref. [1]). Note that the observation of an M - H hysteresis (Fig. 1(a)) is not sufficient evidence for the presence of long-range magnetic order. It is known that [32, 33] in a granular magnetic system with short-range magnetic order, long-ranged dipolar interactions between the grains result in a correlated magnetic response. Such a system can exhibit M - H hysteresis akin to a ferromagnetic-like system, although the system intrinsically does not have any long-range magnetic order. Although we see a hysteretic M - H at low T (Fig. 1(a)), our bulk T - dependent susceptibility measurements reveal a disordered spin glass configuration at low $T < T_{SG}$ (Fig. 1(c)). It is therefore of interest to explore further the magnetic state in our NPs.

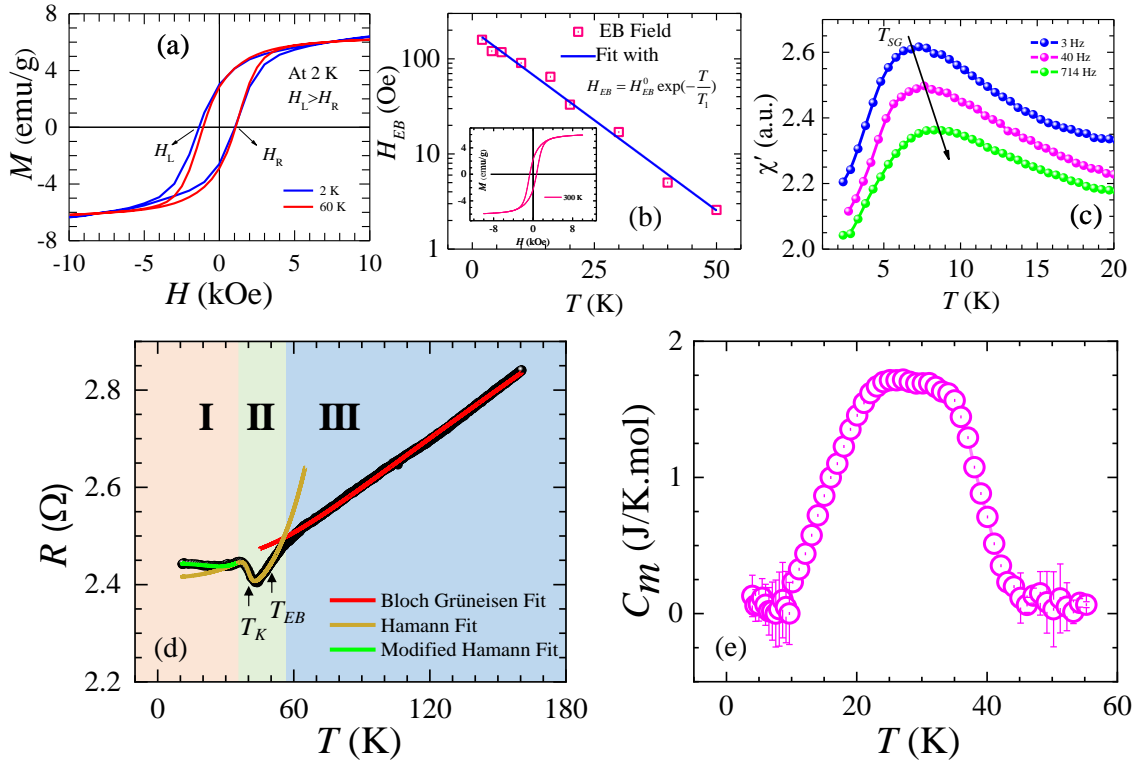


FIG. 1 (a) FC M - H hysteresis loops at 2 K and 60 K. (b) Exchange Bias field (H_{EB}) with temperature in log-linear scale. The solid line is the exponential fit presented in the log-linear scale. The inset shows the M - H hysteresis loop at 300 K (c) Real part (χ') of ac susceptibility with the temperature at different excitation frequencies (f). (d) Resistance (R) as a function of temperature with a constant current of 1

mA flowing through the sample. The data can be divided into three distinct regimes. The solid red curve is the fit to the data in regime III using Bloch Grüneisen function; the solid yellow curve is the fit to the data in regime II with the conventional Hamann equation with contributions from electron-electron and electron-phonon mediated terms included; in regime I, the data has been fitted with the modified Hamann equation along with the term arising from the electron-electron dominated contribution. The solid green curve gives the fit in regime I. See text for details of the fits used. (e) Magnetic contribution (C_m) to the specific heat with temperature.

Electrical and thermal properties of Co₂C nanoparticle pellet:

Figure 1(d) shows the resistance, R versus T measurement (four probes) on the pellet of Co₂C NPs. Four Gold pads were deposited on the pellet for the four-probe measurement. At 170 K the pellet has a resistivity (ρ) = 2×10^{-2} Ω .m, and an residual resistivity ratio, $RRR = R(170 \text{ K})/R(55 \text{ K}) = 1.2$. The relatively high resistivity of Co₂C NPs-pellet compared to a typical metal suggests that the pellet does not follow the theoretical prediction of a paramagnetic metallic nature of bulk Co₂C [27]. Fitting the T dependence of the specific heat of the pellet (C_{sample}) (see Fig. 2 in SI-II) gives a Debye temperature, $\theta_D = 250$ K. Hence as per the specific heat measurements, the T regime from below 170 K until 55 K is associated with strong electron-phonon (e-ph) interactions in the system.

We note from Fig.1(d) that it is not possible to explain the $R(T)$ behavior with one single expression. Therefore the $R(T)$ data in Fig. 1(d) is analysed by dividing it into three distinct regions, viz., regimes I, II and III as seen in Fig.1(d). From the extrapolated coloured lines as shown in Fig.1(d) in the different regimes, note that there is an abrupt change in the curvature of R versus T dependence as one transitions across the regimes. This feature suggests different underlying physical processes become active in the magnetic NP's composite at the transition boundary between the different regimes. We see that above 55 K in region III, the data fits well to the Bloch Grüneisen function (see solid red curve) [34],

$$R(T) = R_0 + A \left(\frac{T}{\theta_D} \right)^5 \int_0^{\theta_D/T} dx. x^5 / [(e^x - 1)(1 - e^{-x})] \quad (1)$$

Here R_0 is the residual resistance due to defect scattering and $\theta_D = 250$ K (as determined from $C_{sample}(T)$). A good fit is obtained in region III with $R_0 = 2.45 \Omega$ and $A = 3.52 \Omega$. The $R(T)$ behaviour suggests a metallic nature with strong electron-phonon scattering dominating the observed $R(T)$ behavior in this regime. Here we would like to mention that the above measurement uncovers the intrinsic metallic nature of Co_2C NPs. This is confirmed as bias dependence of the local density of states (DOS) measured through Scanning Tunneling Microscopy (STM) measurements also reveals the presence of a finite DOS at the Fermi level (see Fig. 3(a) in SI-II), which is characteristic of metallic nature of Co_2C NPs. We have also measured two other pellets made from the Co_2C NPs, and we observe similar $R(T)$ behaviour, thereby confirming that the observed $R(T)$ behaviour is not sample specific. Note that at this juncture, we cannot deduce the extent of grain boundary scattering contribution to $R(T)$. It is likely to be present, however its contribution is subdominant compared to the Bloch Grüneisen mechanism of scattering, which gives a good fit for the $R(T)$ behavior over a wide T window in regime III. The grain boundary scattering however may result in a low RRR (~ 1.2) for our samples.

Below 55 K, which is in the vicinity of T_{EB} ($= 50$ K), the resistance drops sharply to a minimum $R_{min} = 2.4 \Omega$ at ~ 43 K; it increases again to a maximum followed by a secondary minimum before ultimately saturating. The appearance of a minimum in R suggests two possibilities, (i) opening of a bulk gap in the DOS or (ii) electrons getting localized in the material. We first consider the possibility that a minimum feature represents Kondo localization of electrons [35-37]. The Kondo localization is associated with the localization of electrons which screen local magnetic moments present in Co_2C NPs-pellet. The sharp fall below T_{EB} and the consequent

resistance upturn at lower temperatures is fit using two forms. The solid yellow curve in Fig. 1(d) is a fit to the data in regime II using the equation [38]

$$R(T) = R_0 + qT^2 + pT^5 + R_{K0} \left\{ 1 - \frac{\ln\left(\frac{T}{T_K}\right)}{\sqrt{\ln^2\left(\frac{T}{T_K}\right) + s(s+1)\pi^2}} \right\} \quad (2)$$

The first term R_0 here is the constant resistance; the second term arises from contributions due to the usual electron-electron (el-el $\propto T^2$ term) interactions; the third term comes from electron-phonon (el-ph $\propto T^5$ term) interactions, and the last term is the conventional Hamann function corresponding to Kondo localization, where T_K is the Kondo localization temperature. The fit gives $R_0 = 2.33 \, \Omega$, $q = 1.92 \times 10^{-5} \, \Omega \cdot \text{K}^{-2}$, $p = 1.95 \times 10^{-10} \, \Omega \cdot \text{K}^{-5}$, $R_{K0} = 0.04 \, \Omega$, Kondo temperature $T_K = 40.13 \, \text{K}$ and average spin of magnetic site, $s = 3.5 \times 10^{-4}$. By comparing the p and q values in regime II, we see that the contributions from the el-ph interactions are far weaker than the el-el interactions. The resistance upturn can be attributed to the Hamann equation; the competition between this logarithmic increase and the T^2 varying decrement due to the el-el contributions results in the Kondo minimum at $\sim 43 \, \text{K}$. It may be noted that a low value of s is obtained when the Hamann function is used for fitting data for $T < T_K$ [39, 40]. Although the fit captures well the features of the sharp fall and the resistivity upturn above and below the Kondo minimum, respectively, it deviates from the $R(T)$ data below $\sim 35 \, \text{K}$. The solid green curve is the fit to the data below $35 \, \text{K}$ in regime I with the equation

$$R(T) = R_0 + qT^2 + R_{K0} \left\{ 1 - \frac{\ln\left(\frac{\sqrt{T^2 + T_W^2}}{T_K}\right)}{\sqrt{\ln^2\left(\frac{\sqrt{T^2 + T_W^2}}{T_K}\right) + s(s+1)\pi^2}} \right\} \quad (3)$$

It uses R_0 as the constant resistance and includes the usual el-el ($\propto T^2$ term) scattering term giving $R_0 = 2.13 \Omega$, $q = 1.2 \times 10^{-4} \Omega \text{ K}^{-2}$. The last term in the expression is the modified Hamann function [39-42] related to scattering from the Kondo effect and includes the additional contribution associated with Ruderman-Kittel-Kasuya-Yosida (RKKY) interaction. The strength of the RKKY interactions is $k_B T_W$, and an effective temperature replaces the T in the Hamann expression $T_{eff} = \sqrt{T^2 + T_W^2}$. The above expression gives a good fit to the data in regime I with $R_{K0} = 0.19 \Omega$, $T_W = 24.71 \text{ K}$ and $T_K = 40.13 \text{ K}$, and $s = 0.03$, where we obtain using the modified Hamann function a more realistic estimate of s . Note that we also measured the R - T of two other samples (see Figs. 3(b) and 3(c) in SI-II), which exhibit similar behaviour and have resistivity minima at the same temperature. We would like to mention that we have not found a single functional form that gives a continuous fit spanning the three different temperature regimes. Our analysis shows that the strength of the relative contribution of the different scattering terms (values of the fit parameters) gets modified across the different T regimes (see Fig. 1(d)), due to the ‘switching on’ of different effects which modify scattering as the different T boundaries of different regimes are crossed. In regime III at $T > T_{EB}$ the electron – phonon scattering determines the behavior of $R(T)$. However as one enters in regime II, viz., $T < T_{EB}$, with the onset of EB phenomenon there is significant modification to scattering effects and we observe features related to Kondo localization phenomena associated with the strengthening of electron-electron correlation effects, and all of this completely modifies the scattering features upon entering regime II. We also see this clearly demonstrated in regime II, where the dominance of electron-electron scattering effects over electron-phonon scattering effects shows up as the parameter $p \ll q$. With further decrease in T there is strengthening of the electron – electron correlation effects and this results in the emergence of Kondo localization and effects of RKKY correlation contribute to modified scattering at low T in regime I. Therefore in a complex system like Co_2C we see the ‘switching on’ of different

phenomena as the different T regimes are crossed, which in turn significantly modify the nature of scattering events experienced by the electrons in the system. Consequently, the coefficient of the $R(T)$ fit gets modified across the different regimes. In Fig. 1(e), we plot magnetic contribution to the specific heat $C_m(T) = C_{sample}(T) - [C_{Debye}(T) + \gamma T]$, where $C_{Debye}(T) + \gamma T$ is the Debye (phononic) and electronic contribution to specific heat determined by fitting the measured specific heat behaviour of the sample ($C_{sample}(T)$) (see SI-II for details). Concomitant with the evidence of the Kondo effect seen in the electrical transport, the specific heat peak in $C_m(T)$ below T_K (Fig. 1(e)), further supports the Kondo localization scenario in Co₂C NPs-pellet. It is worth noting that T_K is quite close to $T_{EB} = 50$ K, where the EB effect sets in. The appearance of the Kondo effect also suggests that Co₂C is a strongly correlated electronic system. From the fit to $C_{sample}(T)$ (see SI-II), we obtain a high value of Sommerfeld's constant, $\gamma = 74$ mJ/K²mol (note $\gamma \propto g(\epsilon)$, where $g(\epsilon)$ is the DOS at energy ϵ). The enhanced γ value [43-46] suggests the presence of a strong correlation in Co₂C NPs. Our earlier Scanning Tunneling Microscopy (STM) based differential conductance measurements $\frac{dI}{dV} (\propto g(\epsilon))$ in Co₂C NPs- pellet showed a strongly enhanced DOS $g(\epsilon)$, near the Fermi level, ϵ_F (see Fig. 3(a) in SI-II and also Fig. 4(a) inset in ref.[1]; there appears a peak near STM bias voltage = 0 V), which also suggests strong correlations present in Co₂C. DFT calculations on Co₂C reported in our earlier studies [1] do not suggest any bulk gap opening in the system. We also do not see evidence of any gap-like feature in the STM spectra around ϵ_F (see Fig. 3(a) in SI-II). Therefore, opening up of a bulk gap in the DOS is unlikely to be responsible for a minimum in $R(T)$ near T_K . Thus, the above studies show that strong correlation effects in Co₂C NPs is responsible for the onset of Kondo localization at T_K . The Kondo localization appears just below the onset of the EB effect at T_{EB} . Therefore, the nature of resistivity as inferred by the bulk transport measurement is in good agreement with the independent estimations of the local

STM-based differential conductance and the specific heat measurements and therefore establishes the intrinsic material property.

Exploring the magnetic state of Co₂C NP pellet at different T using μ SR studies:

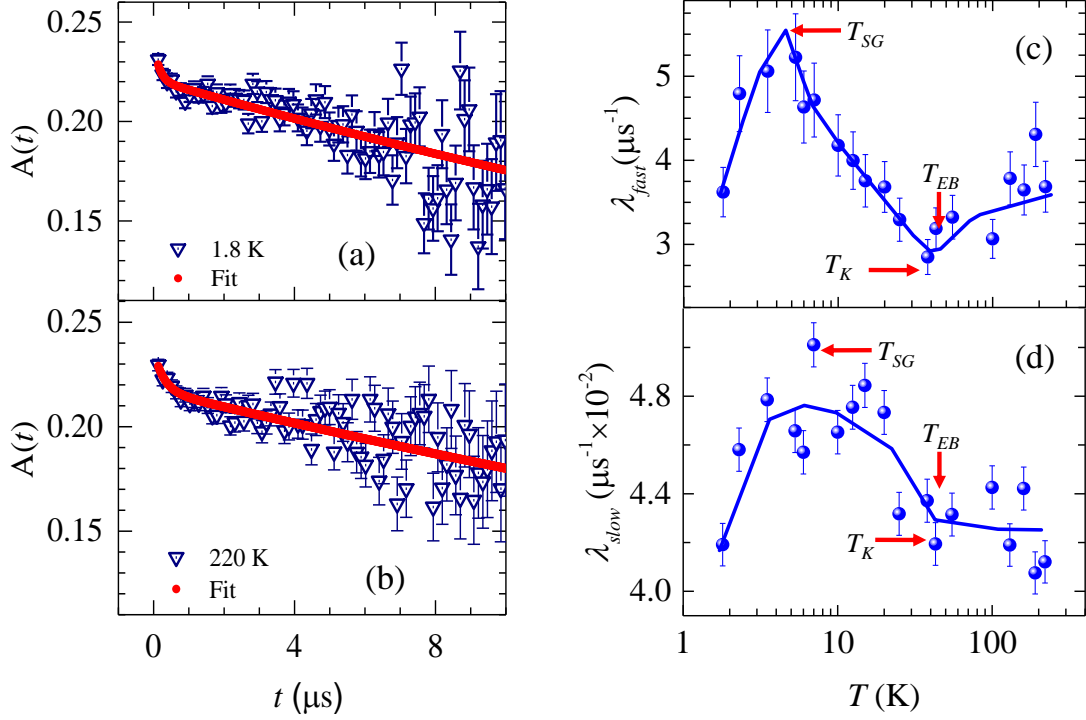


FIG. 2 (a) and (b) show a representative ZF- μ SR time spectra at 1.8 K and 220 K, respectively. The solid lines in the spectra are fit to Eqn. 5. (c) & (d) show the behaviour of relaxation rate of fast & slow components with temperature.

We study the magnetic configuration in the Co₂C NPs- pellet using μ SR measurements. The μ SR measurements were carried out in the temperature range of 1.8 K-220 K using the HiFi spectrometer at ISIS pulsed muon facility, Rutherford Appleton Laboratory, UK [47]. The Co₂C NPs-pellet was loaded onto the standard Ag (99.99%) sample holder used for μ SR due to its time-independent background signal. In our μ SR measurements, fully spin-polarized muons are implanted into the sample, which starts precessing around the local magnetic field present at its stopping site in the magnetically ordered state. The decay of muons to positrons

is recorded with time using forward (F) and backward (B) detectors placed with respect to muons' initial polarization direction. The measured physical quantity, the evolution of muon spin polarization viz., asymmetry, is defined as follows:

$$A(t) = \frac{N_B(t) - \alpha N_F(t)}{N_B(t) + \alpha N_F(t)} \quad (4)$$

$N_B(T)$ and $N_F(T)$ are the number of positron counts in backward and forward detectors at time t , respectively, α is a relative efficiency factor of the two detectors. The value of α ($=1.2870$) was estimated from the small transverse field ($TF = 20$ G) measurements at high temperatures. Figures 2(a) and (b) show the raw zero field (ZF)- μ SR time series $A(t)$ spectra at 1.8 K and 220 K, respectively. The presence of any long-range magnetic order in the sample will produce oscillations in the zero field (ZF) μ SR asymmetry spectrum for a smaller ordered moment but will show a loss of 2/3 of the initial muon asymmetry for a large ordered moment. We observe no oscillatory signal in the ZF- μ SR- $A(t)$ spectra and no loss of the initial asymmetry, which suggests the absence of any long-range magnetic ordering present in the Co₂C NPs-pellet down to 1.8 K [48-50]. We find that the ZF- μ SR- $A(t)$ spectra can be fitted only by using two different relaxation rates. It appears that the sample has one component which relaxes rapidly within the first ~ 1 μ s and another component that relaxes slowly (above ~ 1 μ s). The ZF- μ SR spectra for all T [50-54] are fitted with the following expression,

$$A(t) = A_{BG} + A_{fast} \exp(-\lambda_{fast} t) + A_{slow} \exp(-\lambda_{slow} t) \quad (5)$$

Where λ_{fast} and λ_{slow} are fast and slow components of muon spin relaxation rates. A_{BG} is a constant background, and A_{fast} , and A_{slow} are the corresponding initial asymmetry values, with $A_{fast} \neq A_{slow}$ and $\lambda_{fast} \neq \lambda_{slow}$. The behaviour of λ_{fast} and λ_{slow} is shown in Figs. 2(c), 2(d) in log

scale. We see that λ_{fast} is nearly two orders of magnitude larger than λ_{slow} . The λ_{slow} is however an order of magnitude higher than the background relaxation rate (λ) [55-57] of muons embedded in high purity paramagnetic Ag sample holder. Also note that non monotonic changes in the T dependence of λ_{fast} and λ_{slow} are not characteristic of a paramagnetic state in the Co₂C NP pellet. The two distinct relaxation, λ_{fast} and λ_{slow} rates suggest the presence of two inequivalent muon stopping sites in the NPs target, where the muon experiences different strengths of local magnetic field environment [58, 59].

Muons rapidly precess in the strong local field leading to rapid decay in the ZF asymmetry spectra. Therefore the λ_{fast} for $t < 1 \mu\text{s}$ corresponds to muons embedded in a relatively strong local magnetic field environment in the sample. In contrast, muons that are embedded in an environment with a disordered magnetic configuration, they experience a fluctuating magnetic field with a small average local field. Due to this, the precessional frequency of these muons is low and consequently ZF – asymmetry relaxes slowly with a rate λ_{slow} . The amplitudes, A_{fast} and A_{slow} are proportional to the sample volume fractions for the two muon stopping sites [60]. ZF- μ SR spectra are not very sensitive to the variation in A_{slow} and A_{fast} as a function of temperature. We find them to be almost temperature independent, therefore in all subsequent analyses, we will use the T -independent average value of A_{slow} and A_{fast} . Using the total initial $A(t)$, A_{slow} and A_{fast} values, we calculate the fractions of the average muon population at the two sites. Using this we determine that the fast-relaxing rate is associated with the magnetic fraction having short-range order ($\sim 14\%$ of the sample volume), and the slower relaxation rate is associated with the disordered magnetic fraction ($\sim 86\%$ of the sample volume). It is clear that there is a local magnetic moment distribution inside the sample and the fluctuating magnetic moments do not exhibit onset of long range order down to the T we have studied.

In Fig. 2(c) and 2(d), below 50 K ($\sim T_{EB}, T_K$), the λ_{fast} rapidly increases and reaches a maximum near 5 K which is very close to the SG peak in $\chi'(T)$ at $T_{SG} \sim 6$ K (cf. Fig. 1(c)). For $T < T_{SG}$ viz., in the SG state, the $\lambda_{fast}(T)$ begins to decrease. Due to EB effect, below T_{EB} the fluctuating local magnetic fields in the sample are stabilized and hence the average local field increases. Therefore λ_{fast} shows a pronounced increase from below T_{EB} . Note that the $\lambda_{fast}(T)$ component is sensitive to modifications in the dynamics of these fluctuating local fields, as it shows a cusp-like feature at a T corresponding to the onset of the spin glass phase, viz., at $T = T_{SG}$ (~ 6 K) (see Fig. 2(c)). It is also worth mentioning here that a similar cusp-like feature in $\lambda_{fast}(T)$ has been found near the SG transition in other materials as well [49, 51, 61]. Somewhat similar features as $\lambda_{fast}(T)$ are also shown by $\lambda_{slow}(T)$ values (solid blue line) as well. From the behaviour of $\lambda_{fast}(T)$ and $\lambda_{slow}(T)$ in Fig. 2(c) and 2(d), it appears that in the regime between T_{EB} and T_{SG} , the magnetic environment of the muons is modified compared to that above T_{EB} .

We explore this fluctuating magnetic state in our Co₂C sample further by measuring the local magnetic field distribution at different T 's using transverse field (TF)- μ SR spectra. The TF- μ SR measurements were carried out with the applied field of 20 G at different T . In TF- μ SR geometry, the magnetic field is applied perpendicular to muon's initial spin polarization. Figure 3(a) shows the measured TF- μ SR asymmetry $A(t)$ data captured at 2.3 K (solid black line). The Fast Fourier Transform (FFT) of the measured TF μ SR- $A(t)$ spectra at 2.3 K is shown in Fig. 3(b). The sharp peak in the FFT amplitude at 0.27 MHz corresponds to the externally applied transverse field of 19.92 G. We note that beyond the main peak corresponding to the applied field in Fig. 3(b), there is a broad tail with significant FFT amplitude, which extends up to higher frequencies of about 5 MHz.

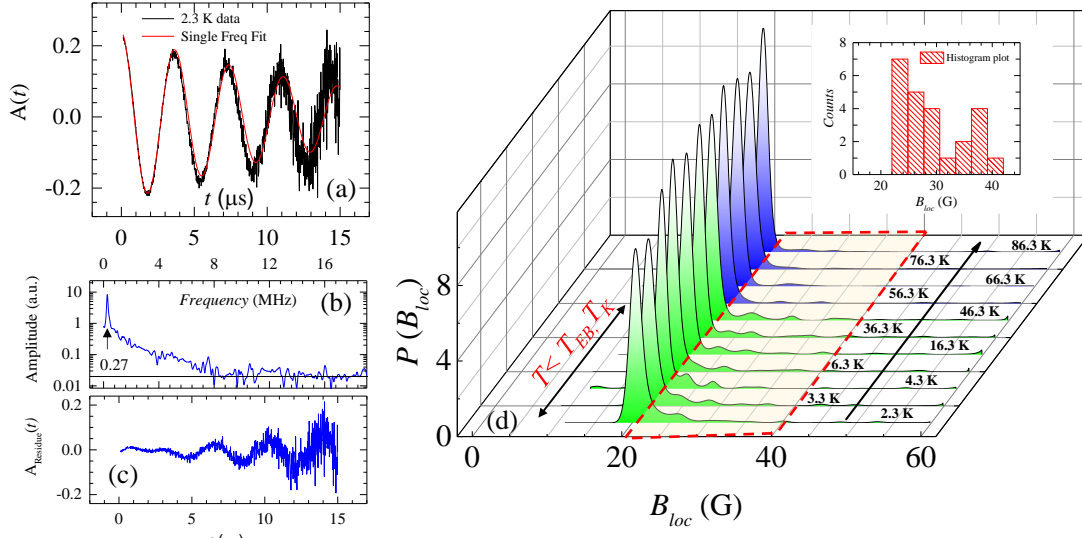


FIG. 3 (a) TF- μ SR spectra at 2.3 K measured in 20 G, the red curve is the fitted data using single frequency (0.27 MHz) in muon decay function, i.e., $F(t) = A \exp(-\lambda_T t) \cos(\omega t + \phi)$, where $\omega = \gamma_\mu B_{loc}$, ϕ is the phase factor, and B_{loc} is the local magnetic field experienced by muons. (b) Fast Fourier Transform of TF- $A(t)$ spectra at 2.3 K shown in Fig. 3(a). (c) The residual asymmetry obtained after fitting of 2.3 K data. (d) Field distribution of the local field in Co_2C NPs at different temperatures, obtained by maximum entropy transformation of the TF- μ SR spectra. The inset shows the histogram plot of the local field values (obtained by counting the number of times of different B_{loc} values observed in the $P(B_{loc})$ peaks below 50 K) inside the sample.

The higher frequencies in the tail correspond to the presence of the local field higher than the applied field inside the sample. We attempt to fit the measured $A(t)$ data in Fig. 3(a) with a single frequency ($\omega = \gamma_\mu B_{loc}$) function of the form $F(t) = A \exp(-\lambda_T t) \cos(\omega t + \phi)$, ϕ is the phase factor. We use $\omega = \gamma_\mu B_{loc} = 0.27$ MHz, obtained from FFT, where $\gamma_\mu = 2\pi \times 135.5342$ MHz/T (in supplementary section III Fig. 4, we plot the residue obtained with a direct fit with $F(t)$ where ω (a fitting parameter) gives a best fit value of 0.275 MHz). The best fit $F(t)$ curve to $A(t)$ is shown in Fig. 3(a), the fit yields values of $A = 0.242$, $\lambda_T = 0.068 \mu\text{s}^{-1}$, and $\phi = 0.077$ rad. In the above expression for $F(t)$, the term $A \exp(-\lambda_T t) = A_{fast} e^{-\lambda_{fast} t} + A_{slow} e^{-\lambda_{slow} t}$. Note that in this expression, over longer time scales, $\lambda_T \sim \lambda_{slow}$, the fast relaxation component decays out within $t \leq 0.5 \mu\text{s}$ (which is far less than even one full period in the TF spectra). In

supplementary section III we show that the by fitting TF data using the approximate, $F(t) = A \exp(-\lambda_T t) \cos(\omega t + \phi)$ form the λ_T is comparable to the λ_{slow} determined from the earlier ZF measurements. In Fig. 3(c), we plot $A_{residue}(t) = A(t) - F(t)$, which shows the presence of significant residual asymmetry using a single frequency (0.275 MHz) in the expression for $F(t)$, to fit the $A(t)$ data. This suggests the insufficiency of using a single frequency, $f = 0.275$ MHz for fitting our data, which inturn suggests including additional frequency components to analyse the TF asymmetry spectra. Note that similar alternative fits used for analysing typical TF- μ SR spectra of the type, $F(t) = A \exp(-\lambda_T t) \exp(-\frac{\sigma^2 t^2}{2}) \cos(\omega t + \phi)$, yields very low values of $\sigma \sim 0.005 \mu s^{-1}$ and we find it does not yield any significantly better fit compared to that in Fig.3(a). Using the modified $F(t)$, oscillations still persist in the $A_{residue}(t)$, similar to that seen in Fig.3(c). The need for incorporating higher frequencies in our analysis of the asymmetry spectra, is further supported by noting the presence of an extended frequency tail above 0.27 MHz in the FFT spectra of Fig. 3(b), indicating additional frequency components contribute to the signal. For this purpose, we use the maximum entropy spectral analysis [62, 63] which captures the presence of higher f components in the TF- μ SR- $A(t)$. Since multiple f 's corresponds to the presence of a distribution of local internal fields, B_{loc} , the analysis gives the distribution $P(B_{loc})$ experienced by the muons (where $\omega = 2\pi f = \gamma_\mu B_{loc}$). Figure 3(d) main panel shows $P(B_{loc})$ versus B_{loc} measured at different T .

In Fig. 3 (d) note that the peak in $P(B_{loc})$ is at 20 G, the applied transverse magnetic field. While at higher T , only the 20 G peak is visible in the $P(B_{loc})$ plot; however, as T is lowered, additional satellite peaks appear in the $P(B_{loc})$ distribution below 50 K ($= T_{EB}$). The peaks in $P(B_{loc})$ above 20 G are more pronounced below $T = 43$ K, which is close to T_K (see the evolution of peaks above 20 G in $P(B_{loc})$ plot inside the red dashed square regions in Fig. 3(d)). From the $P(B_{loc})$ at different T 's, we count the number of times peaks in B_{loc} (>20 G) appear in $P(B_{loc})$. The

histogram of the counts versus B_{loc} is shown in the inset of Fig. 3(d). The distribution of B_{loc} (> 20 G) in the inset of Fig. 3(d) spreads out between ~ 23 G to 40 G. Note that at ISIS the applied TF was set to 20 G with an accuracy of $\sim \pm 1.2$ G. The spread in the applied field is much lower than the field distribution seen in Fig.3(d) inset. Thus, we clearly see that, at $T < 50$ K = T_{EB} , a magnetic state with a broad distribution of local magnetic fields appears in the Co₂C NPs-pellet.

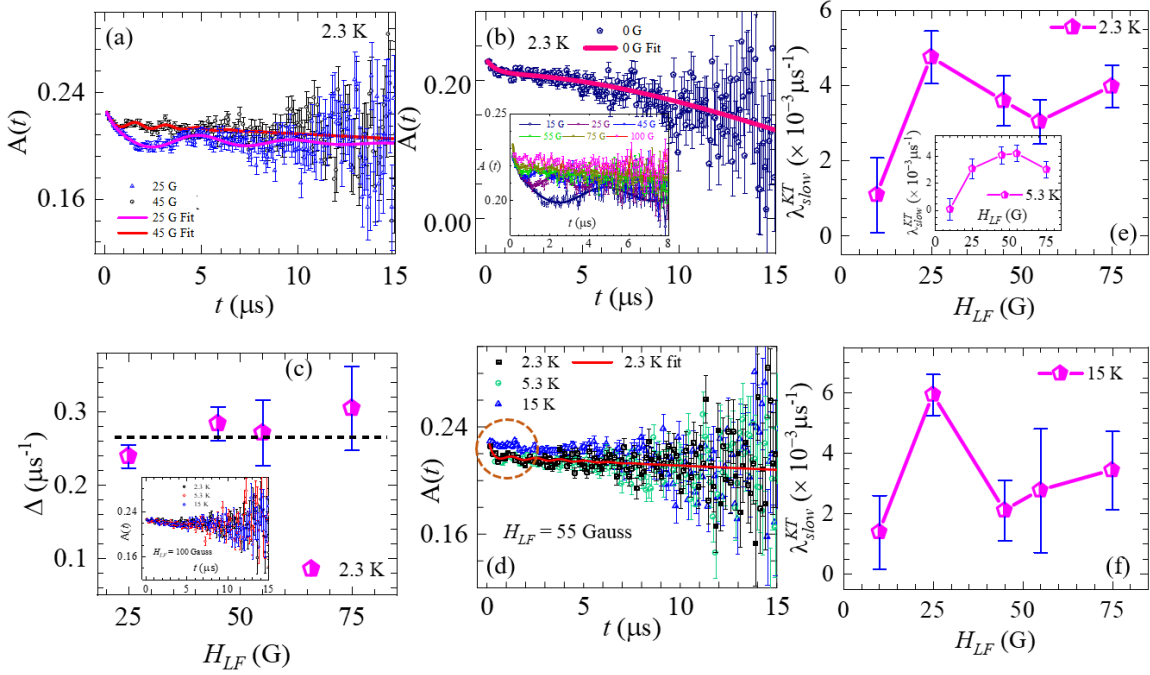


FIG. 4 (a) Longitudinal field (LF) μ SR measurements performed at two different fields of 25 G and 45 G and at 2.3 K. The solid lines are the fits to the data using the static Kubo-Toyabe form (Eqn. 6.) (b) shows the ZF μ SR- $A(t)$ spectra; the solid line is the fit with Eqn. 6. Inset shows the evolution of the spectra under different LF, viz., 15, 25, 45, 55, 75, 100 G and at 2.3 K. (c) Variation of the width of the local field distribution (Δ) with field (H_{LF}), obtained at 2.3 K when fit with Eqn. 6. In the inset is shown the μ SR- $A(t)$ spectra at different temperatures under $H_{LF} = 100$ G. Note that irrespective of temperature, the fast relaxation component is absent (see text for details). (d) shows the longitudinal field (LF) μ SR- $A(t)$ spectra taken at 2.3 K, 5.3 K, and 15 K for $H_{LF} = 55$ G and the fit to 2.3 K data with Eqn. 6 with the solid red line. See that at 2.3K and 5.3 K, the fast and slow relaxing components are clearly seen (see the encircled region) while at 15 K, the fast relaxation is absent. (e) shows the behaviour of relaxation rate of the slow components with H_{LF} at 2.3 K; in the inset is shown relaxation rate of the slow components with H_{LF} at 5.3 K. (f) shows the behaviour of relaxation rate of the slow components with H_{LF} at 15 K;

We now investigate the dynamics of the magnetic fluctuations present in our Co₂C-NP system using longitudinal field (LF) μ SR measurements at 2.3 K ($< T_{SG} = 6$ K). In LF μ SR

measurements, the longitudinal field (H_{LF}) is applied in the direction of muon's spin polarization, the implanted muons precess around the resultant magnetic field, which is the net of H_{LF} and the internal local field at the muon site. For two different applied longitudinal fields, $H_{LF} = 25$ G and 45 G, Fig. 4(a) shows the LF- μ SR asymmetry time-series spectra, $A(t)$, captured at 2.3 K. The progressive loss of decay in $A(t)$ signal with increasing H_{LF} in the inset of Fig.4(b), suggests the muons get strongly polarized along the applied field direction. At large enough fields the muon spins are completely polarised by the applied field and they decouple from the environment as no relaxation in the asymmetry signal is observed [48, 64]. To analyse dynamics of spins the LF- μ SR asymmetry spectra, we use a form based on the well-known Kubo-Toyabe function $G_z(H_{LF}, \Delta, t)$ in the ZF- μ SR- $A(t)$ fitting in Eqn. (5) [59, 60] viz.,

$$A(t) = A_{fast} \exp(-\lambda_{fast}^{KT} t) + A_{slow} \exp(-\lambda_{slow}^{KT} t) \times G_z(H_{LF}, \Delta, t) \quad (6)$$

Where $G_z(H_{LF}, \Delta, t)$ is the static Kubo-Toyabe function (see supplementary SI-III), Δ/γ_μ is the width of the distribution of B_{loc} at the muon sites. Note from Fig. 4(a) that, Eqn. (6) gives a good fit for both 25 G and 45 G LF-spectra's at 2.3 K and Fig. 4(b) shows Eqn. (6) also fits the ZF- μ SR spectra at 2.3 K by setting $H_{LF} = 0$ G in the equation. We find that by fitting the ZF- μ SR spectra obtained at different T using Eqn. (6), yields $\lambda_{fast}^{KT}(T)$, whose magnitude and T behavior are similar to $\lambda_{fast}(T)$ obtained earlier in Fig. 2(c) (see SI section III Fig. 5). Note that the $\lambda_{slow}^{KT}(T)$, which characterizes the long time dynamics of the muons in the local magnetic field environment, is approximately three orders of magnitude smaller than λ_{fast}^{KT} . The T -independent A_{fast} and A_{slow} values are determined from the ZF- μ SR spectra. Figure 4(c) shows the variation of $\Delta(H_{LF})$ at 2.3 K. The nearly constant Δ ($\sim 0.3 \mu\text{s}^{-1}$) with H_{LF} suggests the average width of the distribution of the local field seen by the muon remains almost unchanged in the SG regime with varying H_{LF} . Inset of Fig. 4(c) shows that at 100 G the polarized muons have completely decoupled from their local magnetic environment at all T

and do not show any decay. The $\Delta \sim 0.3 \mu\text{s}^{-1}$ corresponds to an average field spread of ~ 3.5 G. Note that this field spread is much smaller than the spread in B_{loc} determined in inset of Fig. 3(d) through TF measurements. Figure 4(d) shows that $H_{LF} = 55$ Oe is not sufficient to fully polarize the muons and decouple them from their magnetic environment at 2.3 K. The spectra in Fig. 4(d) shows that without changing H_{LF} , increasing T to 15 K leads to the decoupling of muons. The above suggests that at low T there are low-frequency fluctuating magnetic fields arising from magnetically ordered regions in the pellet (possible regions with short range order) with which the muons are coupled.

Figures 4(e) and 4(f) show the dynamics of magnetic fluctuations. By comparing the λ_{slow}^{KT} behaviour above 20 G in Figs. 4(e) and 4(f) we see a drop of $\sim 25\%$ at 15 K compared to the values at 2.3 K or 5.3 K (for $H_{LF} > 20$ G). At 15 K the slow relaxation (low λ_{slow}^{KT} value) in the presence of a relatively high H_{LF} (> 20 G) suggests that muons have decoupled from the local magnetic field environment and they only sense the fluctuating background nuclear field. In a similar H_{LF} range (> 20 G), from 2.3 to 10 K, the muons are coupled to the strong local field environment which is not overcome by the applied H_{LF} and the relaxation rate λ_{slow}^{KT} is comparatively higher which suggests that the fluctuations in the system are low compared to its high temperature (15 K) counterpart [65]. In this low T regime where the Co_2C NP sample host significant local field, further lowering the H_{LF} from 20 G results in a significant drop in λ_{slow}^{KT} (Fig. 4(e)). As the field increases, there is a subsequent slowing down of the dynamical fluctuations in this low temperature regime. The sustained nature of dynamical fluctuations at low T has been seen in f-electron systems and spin glass systems [51, 57, 61, 66-68]. Below the glass freezing temperature where the moments are frozen into a glassy configurations, a significant drop in the muSR relaxation rate has been observed in the past [51, 57]. These results are consistent with our susceptibility studies showing the presence of glassy like phase

below 6 K. It is interesting to note that the temperature and field dependence of λ_{fast}^{KT} also exhibits a comparable behavior to that of λ_{slow}^{KT} (see supplementary information Section IV Fig. 6) due to freezing of spins dynamics as the sample enters the glassy regime at low temperatures ($< T_{SG}$).

Our study of the ZF- μ SR spectra of the fast and slow amplitude in Fig. 2 shows that Co₂C NPs-pellet has about 14% short-range ordered fraction, and 86% is a magnetically disordered fraction. Our rough estimation from fitting the virgin M - H curve at 2 K (see SI-IV for details of the fit), shows that the typical size of the cluster (island) with short-range magnetic order is $\sim 15 \text{ \AA}$ which is much smaller than a single nanoparticle size of $\sim 40 \text{ nm}$. Our μ SR studies have already shown that $\sim 14\%$ of the pellet volume has these islands with short-range order distributed randomly in a sea of disordered spin configurations. The relaxation rate associated with the short-range ordered fraction $\lambda_{fast}(T)$ shows a significant increase between T_{EB} and T_{SG} (Fig. 2(c)). This increase corresponds to the rapid increase in the depolarization rate of the muons, which suggests more interaction between the muons with the local internal fields stabilizing in the sample. Hence the increase in $\lambda_{fast}(T)$ between T_{EB} and T_{SG} corresponds to the short-range ordered magnetic state becoming more stable in the NPs. We believe the increase in $\lambda_{fast}(T)$ and $\lambda_{slow}(T)$ below 50 K signifies the onset of exchange interaction ($J_{EB} = K_B T_{EB}$) at the interface between the fraction with short-range order and magnetically disordered fractions. Thus, at T_{EB} , a magnetic interface forms with the J_{EB} stabilizing at the interface. This J_{EB} couples the magnetically short range-ordered and disordered fractions on two sides of the interface and which in turn helps in stabilizing the local internal fields in the system. As the fluctuations of the random moments decrease below T_{EB} , the strong correlations in Co₂C lead to Kondo screening of the stabilized moments at random sites by the conduction electrons below T_K (Fig. 1(d)). At $T > T_{EB}$, the $R(T)$ behaviour is governed by electron-phonon scattering and there is no

significant magnetic contribution to it. As T is lowered below T_{EB} , strengthening electron-electron correlation effects result in the formation of the Kondo localized states below T_K . This leads to enhanced scattering and $R(T)$ increase. So below T_K the 14 % regions in the pellet with short range magnetic order begin to make their presence felt. At lower $T \ll T_K$, viz., in the RKKY regime, the remaining 86% regions also contribute to the $R(T)$ behavior. Our analysis in Fig. 1(d) shows a crossover from the Kondo-screened scenario to an RKKY interaction-dominated regime. In this regime, the islands with short-range order interact via the RKKY interaction mediated by the conduction electrons. At low T and low fields, the magnetic clusters are coupled by RKKY interactions. Frustration in the interactions possible leads to a frozen spin glass like configuration with very slow dynamics at these low T 's. The λ_{fast} and λ_{slow} significantly decreasing below T_{SG} (Fig. 2(c)) is due to entry into a frozen SG regime, whose evidence is also seen in the LF-muSR results. At $T < T_{EB}$ with the onset of J_{EB} at the interface, the fluctuations of the moments around the interface are suppressed, and the internal local fields are stabilized. As seen in Fig. 3(d), this shows up as a stable broad local field distribution ($P(B_{loc})$) below T_K and T_{EB} . Hence, we propose that in the Co₂C NPs-pellet, a magnetic interface forms below T_{EB} . This interface separates a disordered fraction and a short-range ordered fraction with an exchange interaction that couples the two fractions. The formation of the magnetic interface with J_{EB} below T_{EB} could be triggered by the onset of some additional weak AFM interactions in the system. Earlier DFT work [23] showed that the Co₂C NPs have a structurally ordered core with bulk-like atomic coordination of Co; however, there is a significant increase in the Co atoms with lower coordination near the surface of the NPs. The structurally distorted shell of the NPs may harbour weak AFM interaction whose effect becomes prominent below T_{EB} . This AFM interaction competing with FM interaction in the Co₂C system leads to frustration and transition into an SG state at low $T < T_{SG}$. Note that our NPs-pellet is an agglomeration of grains. Hence there is a complex meandering manifold of

grain boundaries crisscrossing our sample. The grain boundary has no preferred orientation. Thus, the EB effect which arises at such a meandering interface is also unlikely to exhibit any preferred orientation.

In summary, the Co₂C NP pellet system is a complex and strongly interacting system whose presence is revealed through effects that switch on below different characteristic temperature scales. Our ZF μ SR and TF μ SR measurements reveal that the mean-field magnetic landscape of the Co₂C NP pellet can be described as clusters or islands with short-range magnetic order. These islands are embedded in a sea of magnetically disordered medium. The clusters and the surrounding medium have a complex set of interactions coupling them. The first coupling relates to exchange bias interaction which switches on below $T_{EB} = 50$ K. With lowering of T below T_{EB} there are strong electronic correlations effects in Co₂C NP pellet resulting in Kondo Localization to set in below $T_K \sim 40.13$ K. The occurrence of Kondo localization in the T_K regime is found to be near T_{EB} . At lower T ($< T_K$) there are features of another interaction, viz., the RKKY interactions which produce a frozen spin-glass phase at $T < T_{SG}$. Further detailed theoretical and experimental investigations into the complex magnetic character of Co₂C NP pellet:

Acknowledgment: S. S. Banerjee would like to acknowledge the funding support from the Department of Science and Technology (DST), the Government of India and RAL UK program, and IIT Kanpur, DST-SERB SUPRA program. SSB would also like to thank the ISIS Facility for beam time on the HiFi spectrometer, RB1968044. Suprotim Saha acknowledges the Prime Minister's Research Fellows (PMRF) Scheme of the Ministry of Human Resource Development, Govt. of India, for funding support.

References

- [1] Roy N, Ali M A, Sen A, Adroja D T, Sen P and Banerjee S S 2021 Exploring a low temperature glassy state, exchange bias effect, and high magnetic anisotropy in Co₂C nanoparticles *J Phys Condens Matter* **33**
- [2] Silva F G, Depuyrot J, Raikher Y L, Stepanov V I, Poperechny I S, Aquino R, Ballon G, Geshev J, Dubois E and Perzynski R 2021 Exchange-bias and magnetic anisotropy fields in core-shell ferrite nanoparticles *Scientific Reports* **11** 5474
- [3] Golosovsky I V, Salazar-Alvarez G, López-Ortega A, González M A, Sort J, Estrader M, Suriñach S, Baró M D and Nogués J 2009 Magnetic Proximity Effect Features in Antiferromagnetic/Ferrimagnetic Core-Shell Nanoparticles *Physical Review Letters* **102** 247201
- [4] Nogués J, Sort J, Langlais V, Skumryev V, Suriñach S, Muñoz J S and Baró M D 2005 Exchange bias in nanostructures *Physics Reports* **422** 65-117
- [5] Skumryev V, Stoyanov S, Zhang Y, Hadjipanayis G, Givord D and Nogués J 2003 Beating the superparamagnetic limit with exchange bias *Nature* **423** 850-3
- [6] Xi L, Wang Z, Zuo Y and Shi X 2010 The enhanced microwave absorption property of CoFe₂O₄ nanoparticles coated with a Co₃Fe₇-Co nanoshell by thermal reduction *Nanotechnology* **22** 045707
- [7] Zeng H, Li J, Wang Z L, Liu J P and Sun S 2004 Bimagnetic Core/Shell FePt/Fe₃O₄ Nanoparticles *Nano Letters* **4** 187-90
- [8] Estrader M, López-Ortega A, Estradé S, Golosovsky I V, Salazar-Alvarez G, Vasilakaki M, Trohidou K N, Varela M, Stanley D C, Sinko M, Pechan M J, Keavney D J, Peiró F, Suriñach S, Baró M D and Nogués J 2013 Robust antiferromagnetic coupling in hard-soft bi-magnetic core/shell nanoparticles *Nature Communications* **4** 2960
- [9] Iglesias O, Labarta A and Batlle X 2008 Exchange bias phenomenology and models of core/shell nanoparticles *J Nanosci Nanotechnol* **8** 2761-80
- [10] Liu W, Zhong W, Du Y J J o n and nanotechnology 2008 Magnetic nanoparticles with core/shell structures **8** 2781-92
- [11] He X, Wang Y, Wu N, Caruso A N, Vescovo E, Belashchenko K D, Dowben P A and Binek C 2010 Robust isothermal electric control of exchange bias at room temperature *Nat Mater* **9** 579-85
- [12] Prejbeanu I L, Kerekes M, Sousa R C, Sibuet H, Redon O, Dieny B and Nozieres J P 2007 Thermally assisted MRAM *J Phys-Condens Mat* **19** 165218
- [13] Chen X, Hochstrat A, Borisov P and Kleemann W 2006 Magnetoelectric exchange bias systems in spintronics *Applied Physics Letters* **89** 202508
- [14] Meiklejohn W H and Bean C P 1956 New Magnetic Anisotropy *Physical Review* **102** 1413-4
- [15] Yuan S, Xu K, Li Z, Yu L, Kang B and Cao S 2009 Exchange bias and spin glassy behavior in low doped La_{1-x}Sr_xCoO₃ cobaltites *Journal of Applied Physics* **105** 093910
- [16] Chappert C, Fert A and Van Dau F N 2009 *Nanoscience and Technology*: Co-Published with Macmillan Publishers Ltd, UK) pp 147-57
- [17] Nogués J and Schuller I K 1999 Exchange bias *Journal of Magnetism and Magnetic Materials* **192** 203-32
- [18] Ali M, Adie P, Marrows C H, Greig D, Hickey B J and Stamps R L 2007 Exchange bias using a spin glass *Nature Materials* **6** 70-5
- [19] Stamps R L 2000 Mechanisms for exchange bias *Journal of Physics D: Applied Physics* **33** R247-R68
- [20] Winkler E, Zysler R D, Vasquez Mansilla M, Fiorani D, Rinaldi D, Vasilakaki M and Trohidou K N 2008 Surface spin-glass freezing in interacting core-shell NiO nanoparticles *Nanotechnology* **19** 185702
- [21] Schwarzkopf P and Kieffer R 1953 *Refractory hard metals: borides, carbides, nitrides, and silicides; the basic constituents of cemented hard metals and their use as high-temperature materials*: Macmillan)
- [22] Harris V G, Chen Y, Yang A, Yoon S, Chen Z, Geiler A L, Gao J, Chinnasamy C N, Lewis L H, Vittoria C, Carpenter E E, Carroll K J, Goswami R, Willard M A, Kurihara L, Gjoka M and Kalogirou O 2010 High coercivity cobalt carbide nanoparticles processed via polyol reaction: a new permanent magnet material *Journal of Physics D: Applied Physics* **43** 165003
- [23] He Z B, Maurice J L, Gohier A, Lee C S, Pribat D and Cojocaru C S 2011 Iron Catalysts for the Growth of Carbon Nanofibers: Fe, Fe₃C or Both? *Chemistry of Materials* **23** 5379-87
- [24] Host J, Block J, Parvin K, Dravid V, Alpers J, Sezen T and LaDuca R 1998 Effect of annealing on the structure and magnetic properties of graphite encapsulated nickel and cobalt nanocrystals *Journal of Applied Physics* **83** 793-801
- [25] Chen J G 1996 Carbide and Nitride Overlayers on Early Transition Metal Surfaces: Preparation, Characterization, and Reactivities *Chem Rev* **96** 1477-98

- [26] Zhang Y, Chaubey G S, Rong C, Ding Y, Poudyal N, Tsai P-c, Zhang Q and Liu J P 2011 Controlled synthesis and magnetic properties of hard magnetic Co_xC ($x=2, 3$) nanocrystals *Journal of Magnetism and Magnetic Materials* **323** 1495-500
- [27] Zhao Y-H, Su H-Y, Sun K, Liu J and Li W-X 2012 Structural and electronic properties of cobalt carbide Co_2C and its surface stability: Density functional theory study *Surface Science* **606** 598-604
- [28] Carroll K J, Huba Z J, Spurgeon S R, Qian M, Khanna S N, Hudgins D M, Taheri M L and Carpenter E E 2012 Magnetic properties of Co_2C and Co_3C nanoparticles and their assemblies *Applied Physics Letters* **101** 012409
- [29] Shen X, Zhang T, Suo H, Yan L, Huang L, Ma C, Li L, Wen X, Li Y and Yang Y 2020 A facile one-pot method for synthesis of single phase Co_2C with magnetic properties *Materials Letters* **271** 127783
- [30] Roy N, Sen A, Sen P and Banerjee S S 2020 Localized spin waves at low temperatures in a cobalt carbide nanocomposite *Journal of Applied Physics* **127** 124301
- [31] Mydosh J A 1978 Spin glasses — recent experiments and systems *Journal of Magnetism and Magnetic Materials* **7** 237-48
- [32] Luttinger J M and Tisza L 1946 Theory of Dipole Interaction in Crystals *Physical Review* **70** 954-64
- [33] Allia P, Coisson M, Knobel M, Tiberto P and Vinai F 1999 Magnetic hysteresis based on dipolar interactions in granular magnetic systems *Physical Review B* **60** 12207-18
- [34] Ziman J M 2001 *Electrons and phonons: the theory of transport phenomena in solids*: Oxford university press)
- [35] Barua S, Hatnean M C, Lees M R and Balakrishnan G 2017 Signatures of the Kondo effect in VSe_2 *Scientific Reports* **7** 10964
- [36] Herrera W T, Xing Y T, Ramos S M, Munayco P, Fontes M B, Baggio-Saitovitch E M and Litterst F J 2011 Kondo effect and spin-glass behavior of dilute iron clusters in silver films *Physical Review B* **84** 014430
- [37] Kalvius G M, Kratzer A, Noakes D R, Munch K H, Wappling R, Tanaka H, Takabatake T and Kiefl R F 1995 Spin Freezing in the Kondo Metal CePtSn *Europhys Lett* **29** 501-6
- [38] Zhang H, Zhang H, Yan X, Zhang X, Zhang Q, Zhang J, Han F, Gu L, Liu B, Chen Y, Shen B and Sun J 2017 Highly Mobile Two-Dimensional Electron Gases with a Strong Gating Effect at the Amorphous $\text{LaAlO}_3/\text{KTaO}_3$ Interface *ACS Applied Materials & Interfaces* **9** 36456-61
- [39] Nagaoka Y 1965 Self-Consistent Treatment of Kondo's Effect in Dilute Alloys *Physical Review* **138** A1112-A20
- [40] Ding X, Xing J, Li G, Balicas L, Gofryk K and Wen H-H 2021 Crossover from Kondo to Fermi-liquid behavior induced by high magnetic field in 1T-VTe_2 single crystals *Physical Review B* **103** 125115
- [41] Kästner J and Wassermann E F 1977 Kondo effect and impurity interactions in the resistivity of dilute ZnMn alloys *Journal of Low Temperature Physics* **29** 411-29
- [42] Wang Y H, Xie C Z, Li J B, Du Z, Cao L, Han Y Y, Zu L, Zhang H C, Zhu H M, Zhang X Y, Xiong Y M and Zhao W S 2021 Weak Kondo effect in the monocrystalline transition metal dichalcogenide ZrTe_2 *Physical Review B* **103** 174418
- [43] Tsujii N, Kontani H and Yoshimura K 2005 Universality in Heavy Fermion Systems with General Degeneracy *Physical Review Letters* **94** 057201
- [44] Das D, Gruner T, Pfau H, Paramanik U B, Burkhardt U, Geibel C and Hossain Z 2014 Heavy fermion and Kondo lattice behavior in the itinerant ferromagnet CeCrGe_3 *Journal of Physics: Condensed Matter* **26** 106001
- [45] Tsujii N, Yoshimura K and Kosuge K 2003 Deviation from the Kadowaki Woods relation in Yb-based intermediate-valence systems *Journal of Physics: Condensed Matter* **15** 1993-2003
- [46] Michor H, Berger S, El-Hagary M, Paul C, Bauer E, Hilscher G, Rogl P and Giester G 2003 Crystal structure and Kondo lattice behavior of CeNi_9Si_4 *Physical Review B* **67** 224428
- [47] Walker D C 2009 *Muon and Muonium Chemistry*: Cambridge University Press)
- [48] Blundell S J 1999 Spin-polarized muons in condensed matter physics *Contemp Phys* **40** 175-92
- [49] Hayano R S, Uemura Y J, Imazato J, Nishida N, Yamazaki T and Kubo R 1979 Zero-and low-field spin relaxation studied by positive muons *Physical Review B* **20** 850-9
- [50] Bert F, Mendels P, Olariu A, Blanchard N, Collin G, Amato A, Baines C and Hillier A D 2006 Direct evidence for a dynamical ground state in the highly frustrated $\text{Tb}_2\text{Sn}_2\text{O}_7$ pyrochlore *Phys Rev Lett* **97** 117203
- [51] Yadav P, Sharma S, Baker P J, Biswas P K, da Silva I, Raghunathan R, Deshpande U, Choudhary R J, Lalla N P and Banerjee A 2019 μSR and neutron diffraction studies on the tuning of spin-glass phases in the partially ordered double perovskites $\text{SrMn}_{1-x}\text{W}_x\text{O}_3$ *Physical Review B* **99** 214421
- [52] Colman R H, Manuel P, Khalyavin D D, Hillier A D and McLaughlin A C 2013 Spin dynamics in $\text{IrSr}_2\text{Sm}_{1.15}\text{Ce}_{0.85}\text{Cu}_2\text{O}_{10}$: Complex magnetic behavior in a layered iridocuprate *Physical Review B* **88** 184408

- [53] Uemura Y J, Keren A, Kojima K, Le L P, Luke G M, Wu W D, Ajiro Y, Asano T, Kuriyama Y, Mekata M, Kikuchi H and Kakurai K 1994 Spin fluctuations in frustrated kagome lattice system $\text{SrCr}_8\text{Ga}_4\text{O}_{19}$ studied by muon spin relaxation *Phys Rev Lett* **73** 3306-9
- [54] Dalmas de Reotier P, Yaouanc A, Keller L, Cervellino A, Roessli B, Baines C, Forget A, Vaju C, Gubbens P C, Amato A and King P J 2006 Spin dynamics and magnetic order in magnetically frustrated $\text{Tb}_2\text{Sn}_2\text{O}_7$ *Phys Rev Lett* **96** 127202
- [55] de Réotier P D, Huxley A, Yaouanc A, Flouquet J, Bonville P, Imbert P, Pari P, Gubbens P C M and Mulders A M 1995 Absence of zero field muon spin relaxation induced by superconductivity in the B phase of UPt_3 *Physics Letters A* **205** 239-43
- [56] Bueno J F, Arseneau D J, Bayes R, Brewer J H, Faszler W, Hasinoff M D, Marshall G M, Mathie E L, Mischke R E, Morris G D, Olchanski K, Selivanov V and Tacik R 2011 Longitudinal muon spin relaxation in high-purity aluminum and silver *Physical Review B* **83** 205121
- [57] Yaouanc A and De Reotier P D 2011 *Muon spin rotation, relaxation, and resonance: applications to condensed matter*: Oxford University Press)
- [58] Basini M, Sanna S, Orlando T, Bordonali L, Cobianchi M, Arosio P, Mariani M, Peddis D, Bonanni V, Mathieu R, Kalaivani T, Singh G, Larionova J, Guari Y, Lartigue L and Lascialfari A 2020 Low-temperature anomalies in muon spin relaxation of solid and hollow $\gamma\text{-Fe}_2\text{O}_3$ nanoparticles: A pathway to detect unusual local spin dynamics *Physical Review B* **102** 195424
- [59] Watanabe I, Akoshima M, Koike Y and Nagamine K 1999 Anomalous slowing down of Cu-spin fluctuations observed by muon spin relaxation in the Zn-substituted $\text{Bi}_2\text{Sr}_2\text{Ca}_{1-x}\text{Y}_x(\text{Cu}_{1-y}\text{Zn}_y)_2\text{O}_{8+\delta}$ system around the hole concentration of 18 per Cu *Physical Review B* **60** R9955-R8
- [60] Watanabe I, Akoshima M, Koike Y, Ohira S and Nagamine K 2000 Muon-spin-relaxation study on the Cu-spin state of $\text{Bi}_2\text{Sr}_2\text{Ca}_{1-x}\text{Y}_x(\text{Cu}_{1-y}\text{Zn}_y)_2\text{O}_{8+\delta}$ around the hole concentration of 18 per Cu *Physical Review B* **62** 14524-30
- [61] Hiroi M, Hisamatsu T, Suzuki T, Ohishi K, Ishii Y and Watanabe I 2013 Muon spin relaxation study of spin-glass freezing in the Heusler compound $\text{Ru}_{1.9}\text{Fe}_{0.1}\text{CrSi}$ *Physical Review B* **88** 024409
- [62] Biswas P K, Rybakov F N, Singh R P, Mukherjee S, Parzyk N, Balakrishnan G, Lees M R, Dewhurst C D, Babaev E, Hillier A D and Paul D M 2020 Coexistence of type-I and type-II superconductivity signatures in ZrB_{12} probed by muon spin rotation measurements *Physical Review B* **102** 144523
- [63] Singh D, Biswas P K, Yoon S, Lee C, Hillier A, Singh R, Singh A Y and Choi K-Y 2019 Coexistence of type-I and type-II superconductivity in topological superconductor PdTe_2 *arXiv preprint arXiv:13773*
- [64] Hachitani K, Fukazawa H, Kohori Y, Watanabe I, Sekine C and Shirota I 2006 Evidence for magnetic ordering associated with metal-insulator transition in $\text{SmRu}_4\text{P}_{12}$ studied by muon spin relaxation *Physical Review B* **73** 052408
- [65] Biswas P K, Salman Z, Neupert T, Morenzoni E, Pomjakushina E, von Rohr F, Conder K, Balakrishnan G, Hatnean M C, Lees M R, Paul D M, Schilling A, Baines C, Luetkens H, Khasanov R and Amato A 2014 Low-temperature magnetic fluctuations in the Kondo insulator SmB_6 *Physical Review B* **89** 161107
- [66] Yaouanc A, Réotier P D, Bonville P, Lebras G, Gubbens P C M, Mulders A M and Kunii S 1999 Dynamical magnetic correlations in the Kondo insulator YbB_{12} *Europhys Lett* **47** 247
- [67] Yaouanc A, de Réotier P D, Glazkov V, Marin C, Bonville P, Hodges J A, Gubbens P C M, Sakarya S and Baines C 2005 Magnetic Density of States at Low Energy in Geometrically Frustrated Systems *Physical Review Letters* **95** 047203
- [68] Yaouanc A, Dalmas de Réotier P, Chapuis Y, Marin C, Vanishri S, Aoki D, Fåk B, Regnault L P, Buisson C, Amato A, Baines C and Hillier A D 2011 Exotic transition in the three-dimensional spin-liquid candidate $\text{Tb}_2\text{Ti}_2\text{O}_7$ *Physical Review B* **84** 184403

Probing the strongly correlated magnetic state of Co₂C nanoparticles at low temperatures using μ SR

Nirmal Roy¹, P C Mahato¹, Suprotim Saha¹, M. Telling², J. S. Lord², D T Adroja^{2,3}, S. S. Banerjee^{1,+}

¹*Indian Institute of Technology Kanpur, Kanpur, Uttar Pradesh 208016, India*

²*ISIS Facility, Rutherford Appleton Laboratory, Chilton, Didcot Oxon OX11 0QX, United Kingdom*

³*Highly Correlated Matter Research Group, Physics Department, University of Johannesburg, P.O. Box 524, Auckland Park 2006, South Africa*

Supplementary Information Section I:

Sample Preparation:

Samples are prepared using the one-pot polyol reduction process [1]. First, we dissolved 1.02 g of NaOH in 20 ml tetraethylene glycol (TEG) in a container by heating it to 100 °C. Another 30 ml of TEG is taken into a 100 ml European flask containing 2.5 mmol of Co (CH₃CO₂)₂·4 H₂O and 0.75 g of polyvinylpyrrolidone (PVP). A magnetic stirrer is then used to mix the mixture for 20 minutes at room temperature. The solution is then poured into the European flask, and the mixture is heated to 373 K for 30 minutes to eliminate the water. The solution is heated further to the boiling point of TEG (583 K) for 1 h. The solution is allowed to cool spontaneously to room temperature. The solution is then diluted with ethanol, and the precipitated nanoparticles (NPs) are extracted from the solution with a rare earth magnet. The leftover solution is drained, and the precipitate is washed with ethanol many times. The

extracted NPs are dried in a vacuum oven, and the powders are compacted into pellets. The pellets do not have any preferred orientation because they are made up of NPs of size of ~ 40 nm.

Sample Characterization:

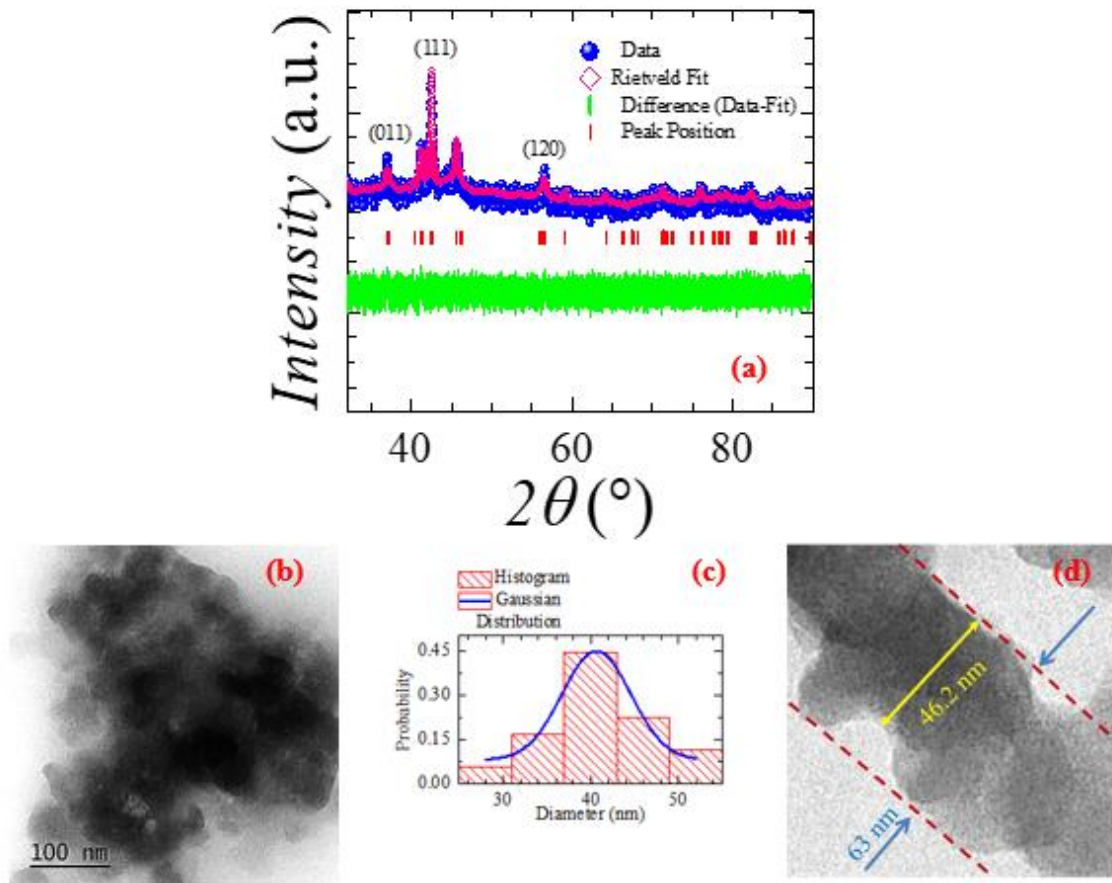


Figure 1. (a) X-ray powder diffraction pattern of Co_2C -NPs. (b) TEM image of the synthesised nanoparticles. (c) Histogram plot of particle size distribution and Gaussian fit to the distribution giving average particle diameter of (40 ± 7.8) nm where the standard deviation of Gaussian fit is 7.8 nm. (d) TEM image of a line of agglomerated NPs.

X-ray diffractions (XRD) are performed to determine the phase and crystal structure. XRD analysis using Rietveld refinement method are shown in Fig. 1(a) confirming the presence of pure Co_2C phase with orthorhombic crystal structure (see Ref. [1] for details). X-ray studies of our sample show that the X-ray diffraction (XRD) peaks are sharp (see Fig. 1(a)). We use the

XRD peak width to estimate the average particle size of the NPs using the Debye Scherrer equation $D = \frac{\xi\lambda}{\beta \cos\theta}$, where D is the average crystallite size. The parameter ξ is the dimensionless shape factor ~ 0.9 , λ ($= 0.15406$ nm for Cu $K\alpha$) is the X-ray wavelength, β is the full width at half maximum of XRD peak, and θ is the Bragg angle. Using the value of $2\theta = 42.5^\circ$ and $\beta = 0.28^\circ$, we estimate $D = (30.7 \pm 7)$ nm. Some of these detailed morphological characterizations of the as-synthesised Co₂C NPs were already presented in our earlier paper [1]. The TEM image of synthesised nanoparticles and histogram plot of particle size are shown in Fig. 1(b) and (c) to determine the average particle size. The average particle size is (40 ± 7.8) nm, where 7.8 nm is the standard deviation (SD) of Gaussian fit. Because of their magnetic nature, individual Co₂C nanoparticles aggregate, making it impossible to get images of individual nanoparticles. A single line of agglomerated particles is depicted in Fig. 1(d) above. The typical diameter of the nanoparticles is of the order (40 ± 7.8) nm, as shown in Fig. 1(d).

Supplementary Information Section II:

Heat Capacity Measurements:

We measured the temperature dependence of specific heat of the Co₂C nanoparticles (NPs) and the background from the sample holder and the system without the sample. First, we measure the heat capacity of the background without the sample. For our background measurements, on the sample holder, instead of the sample, we place the amount of apiezon grease necessary to glue our sample to the holder. The specific heat of the sample (C_{sample}), shown in the Fig. 2(a) below, is obtained by subtracting the background specific heat from the total specific heat measured with the sample. $C_{sample}(T)$ is analyzed to determine the magnetic contribution to specific heat. The total specific heat of the sample is

$$C_{sample} = C_{Debye}(T) + \gamma T + C_m(T) \quad (1)$$

where $C_{Debye}(T) = \frac{9nR}{\left(\frac{\theta_D}{T}\right)^3} \int_0^{\frac{\theta_D}{T}} \left(\frac{x^4 \exp(x)}{(\exp(x)-1)^2} \right) dx$, n and R are number density in a single formula

unit of the material and molar gas constant, θ_D is Debye temperature, and $C_m(T)$ is the magnetic contribution to specific heat while γ is the Sommerfeld's constant. We break up the specific heat data into two temperature regimes, namely, regime (i) below 20 K, where the specific heat behaviour is governed essentially by the electronic contribution, and (ii) above 50 K, where the phononic contribution dominates. Based on the fitting parameters obtained in these regimes, we show the plot of the function $C_{Debye}(T) + \gamma T$ in Fig. 2(a) below. From the fit, we have obtained a $\gamma \sim (74 \pm 10)$ mJ/K².mole and $\theta_D = 250$ K. In Fig. 2(b) below, we determine the magnetic contribution to specific heat using $C_m(T) = C_{sample} - [C_{Debye}(T) + \gamma T]$. It is clear that there is a significant increase in the magnetic contribution to specific heat, which occurs below 40 K, corresponding to the onset of the Kondo effect in the NPs.

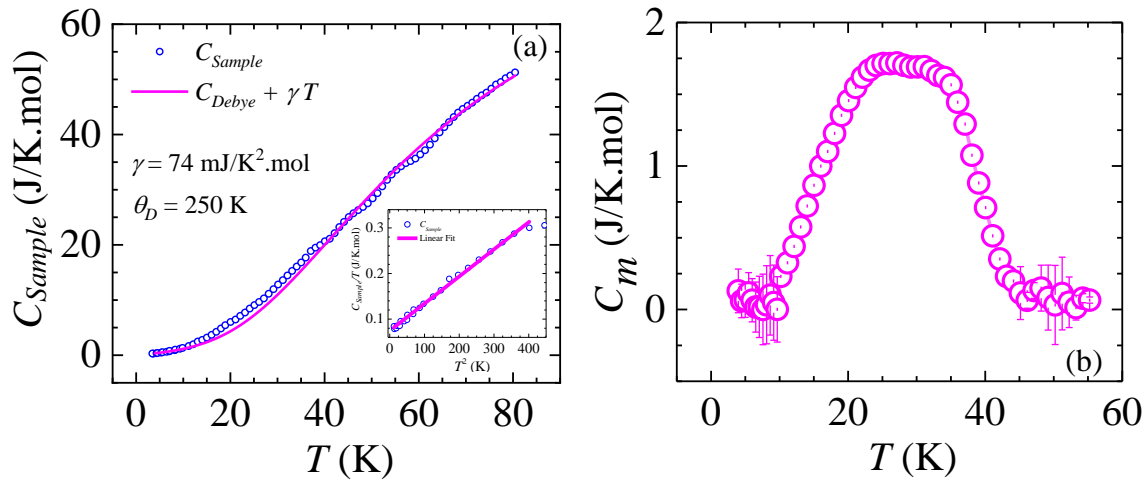


Figure 2. (a) shows temperature dependence of specific heat of the Co₂C NPs fitted with $C_{Debye}(T) + \gamma T$. γ has been determined from the linear fit of the specific heat data at $T < 21$ K ;see inset. (b) shows the magnetic contribution to the specific heat.

Scanning Tunneling Microscopy (STM) Measurements:

STM measurements are performed using a Quazar Technologies room temperature STM (NanoRev. 4.0). The average of 15 measurements of differential conductance dI/dV (\propto density of state (DOS)) is performed as a function of bias voltage V (-0.8 to 0.8 V) at 300 K, and I is the tunneling current. The Figure 3(a) below shows enhanced dI/dV (\propto DOS) at Fermi energy ϵ_F ($V = 0$). The DOS shows absence of any gap at the Fermi Level and the metallic nature of Co_2C NPs. The error bars represent the extent of scatter in the measured local DOS, obtained from doing measurements at different locations on the pellet.

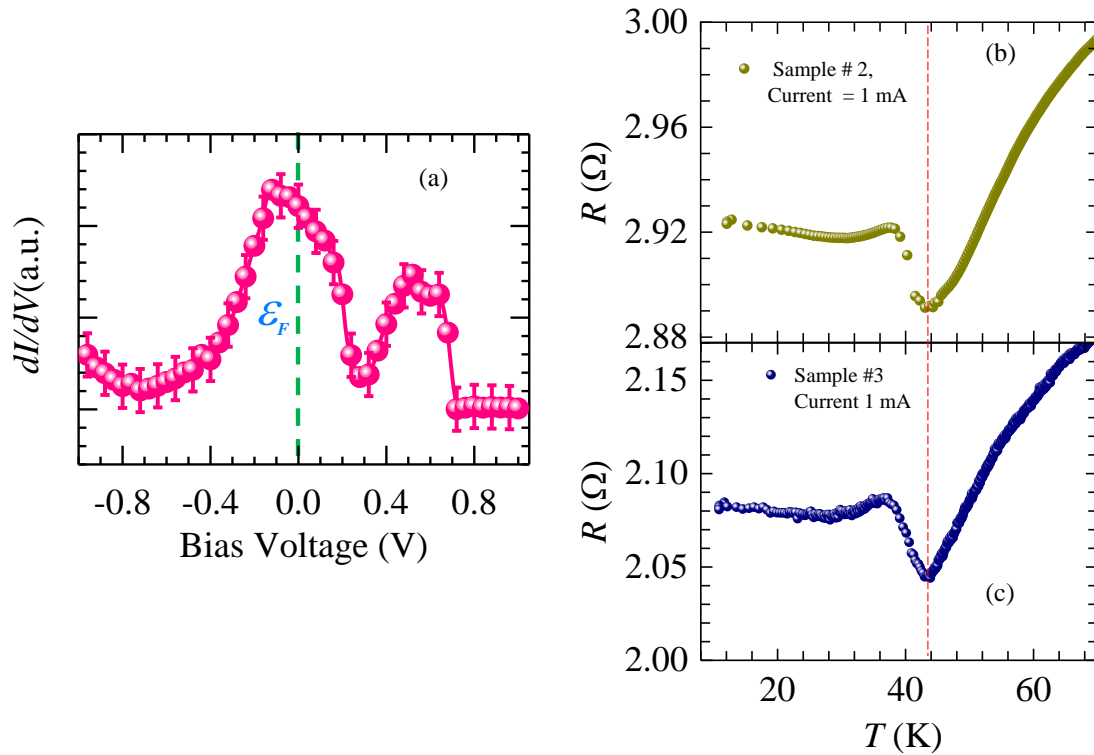


Figure 3. (a) shows the average of 15 measurements of differential conductance dI/dV (\propto DOS) measured on Co_2C NPs of size 40 nm as a function of bias voltage V at 300 K, and I is the tunneling current. (b) and (c) shows R - T of samples #2 and #3 of Co_2C NPs-pellets. Both pellets show similar behavior with a resistivity minimum at the same temperature (red dashed line).

We also measured the R - T of two other samples (see Figs. 3(b) and (c)), which exhibit similar behavior and have resistivity minima at the same temperature. This confirms that the features seen in the resistivity measurement are not sample-dependent.

Supplementary Information Section III:

Single frequency fit of Transverse field (TF) data:

The TF asymmetry spectra at 2.3 K is fitted with the function $F(t) = A \exp(-\lambda_T t) \cos(\omega t + \phi)$ and we keep ω as a free fitting parameter. The fit gives a value of $\omega = 0.275$ MHz, which is close to the FFT peak at 0.27 MHz (see Fig, 3(b) in manuscript). Despite allowing the frequency to vary in the fit, it still shows a considerable residual asymmetry (see Fig. 4 below).

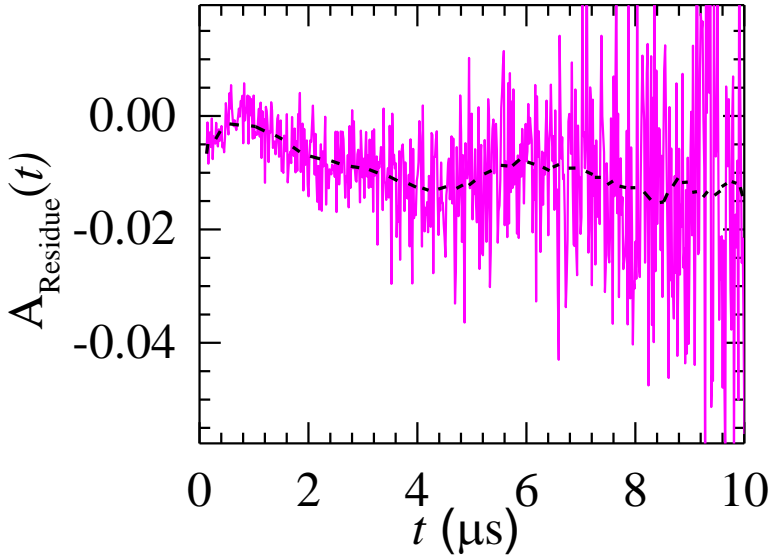


Figure 4: shows the residual asymmetry of fit. The black dashed curve represents the modulating trend of the 50 point adjacent average value of the residue. The modulation in the average value of residue shows the inadequacy of a single frequency fit for the transverse asymmetry data.

Comparison of slow relaxing component obtained from ZF and TF spectra.

In our main manuscript (see Fig. 3(a)) we had used a model $F(t) = A \exp(-\lambda_T t) \cos(\omega t + \phi)$ to fit the TF asymmetry data. It may be noted that the term $A \exp(-\lambda_T t) = A_{fast} \exp(-\lambda_{fast} t) + A_{slow} \exp(-\lambda_{slow} t)$. Note that the dominant contribution $A \exp(-\lambda_T t)$ will be from the slow relaxation term as the fast relaxation component decays out within $t \leq 0.5 \mu s$. The

residue plot in the Fig. 3(c) of our manuscript had suggested that $F(t)$ fit to TF data in Fig. 3(a) is not the best fit, as there are additional frequency components which are present in the data. We have described this further in detail in our MS. we have evaluated the value of λ_T at different T using the above $F(t)$ and compared them with the λ_{slow} values obtained from ZF data in the table below. To within order of magnitude we find a fairly close agreement between the λ_T and λ_{slow} values despite the limited validity of the $F(t)$ function to describe the TF data.

| Temperature (K) | λ_T from F(t) fit from TF data (μs^{-1}) | λ_{slow} from ZF data (μs^{-1}) |
|-----------------|---|--|
| 2.3 | 0.057 ± 0.001 | 0.0458 ± 0.0009 |
| 5.3 | 0.042 ± 0.001 | 0.0466 ± 0.0009 |
| 13 | 0.0472 ± 0.001 | 0.0476 ± 0.0009 |
| 15 | 0.0475 ± 0.001 | 0.0484 ± 0.0009 |

Zero Field (ZF) and Longitudinal Field Kubo Toyabe (KT) Function

In zero-field condition, the static Kubo Toyabe (KT) function is given by

$$G_Z(t) = A \left[\frac{1}{3} + \frac{2}{3} (1 - \Delta^2 t^2) e^{-(1/2)\Delta^2 t^2} \right]$$

where A is the muon asymmetry spectra at time $t = 0$ and Δ is the local field distribution. In the presence of a longitudinal field $\mu_0 H_{LF} = \frac{\omega_0}{\gamma_\mu}$, where ω_0 is the muon's Larmor frequency corresponding to the magnetic field that it experiences and γ_μ is the muon's gyromagnetic ratio, the static Kubo Toyabe function gets modified as [2, 3];

$$G_Z(t) = A \left[1 - \frac{2 \Delta^2}{\omega_0^2} (1 - \cos(\omega_0 t) e^{-(1/2)\Delta^2 t^2}) + 2 \frac{\Delta^4}{\omega_0^4} \omega_0 \int_0^\tau \sin(\omega_0 \tau) e^{-(1/2)\Delta^2 t^2} d\tau \right]$$

Fitting ZF μ SR Data with Static Kubo Toyabe (KT) Function :

We fit the ZF μ SR $A(t)$ spectra with the combination of a fast-relaxing component and slow relaxing component multiplied by Zero Field Kubo Toyabe (KT) function as given below

$$A(t) = A_{fast} e^{-\lambda_{fast}^{KT} t} + A_{slow} e^{\lambda_{slow}^{KT} t} \left\{ \frac{1}{3} + \frac{2}{3} (1 - \Delta^2 t^2) \exp(-1/2 \Delta^2 t^2) \right\}$$

Where A_{fast} , $\lambda_{\text{fast}}^{KT}$, A_{slow} , $\lambda_{\text{slow}}^{KT}$ are the asymmetry and relaxation rate of the fast and slow components, respectively; the term within curly bracket is the zero-field static KT function where δ is the spread of the local field distribution. During fitting we have fixed A_{fast} , A_{slow} at their high temperature values as they do not seem to vary appreciably with temperature. Here, we show the variation of $\lambda_{\text{fast}}^{KT}(T)$; it shows a dip around T_{EB} and T_{K} and then rises sharply to a hump around T_{SG} . Therefore, $\lambda_{\text{fast}}^{KT}$ captures well the characteristic temperature scales of the system.

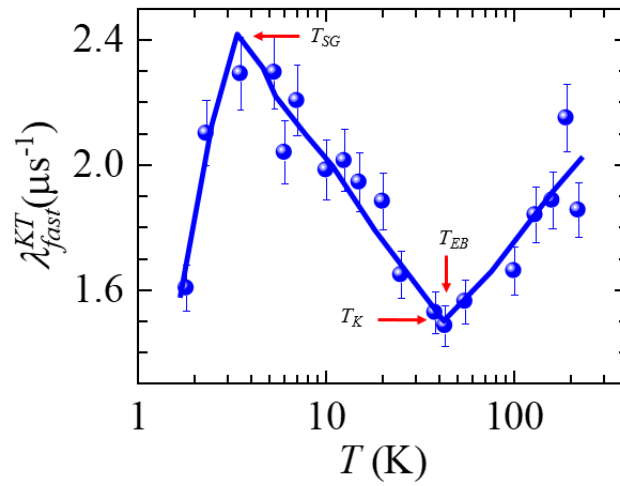


Figure 5. Variation of $\lambda_{\text{fast}}^{KT}$ as a function of temperature

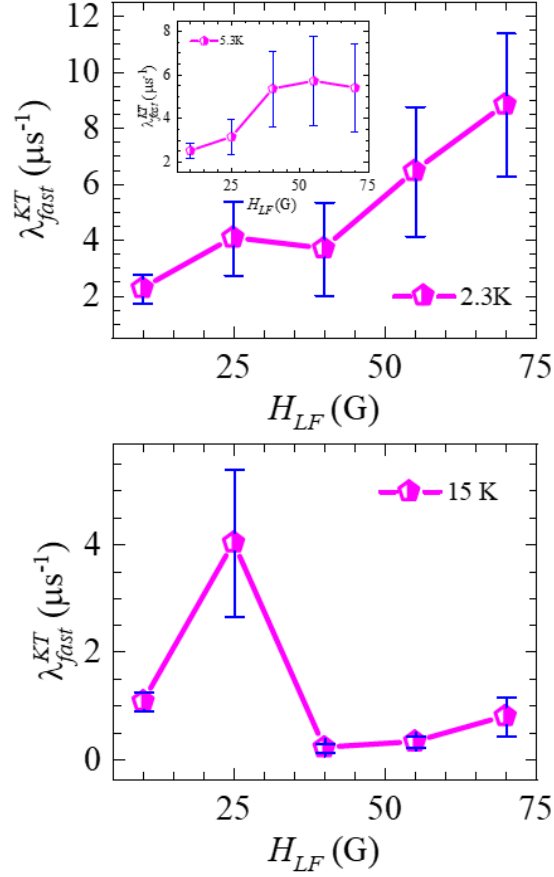


Figure 6. (a) Variation of λ_{fast}^{KT} with H_{LF} at 2.3 K; inset shows the λ_{fast}^{KT} with H_{LF} at 5.3 K. (b) Variation of λ_{fast}^{KT} with H_{LF} at 15 K

Above shows the relaxation rate of the fast component in the LF- μ SR spectra, viz., λ_{fast}^{KT} (see eqn. 6) in the main MS. As T changes from 2.3 K to 15 K, Figs. 6(a) and (b), show that at higher fields e.g., at 55 Oe, there is a significant drop in relaxation rate [4] from about $7 \mu s^{-1}$ to less than $1 \mu s^{-1}$. At higher T (15 K) and higher H_{LF} , the muons decouple from the local magnetic field environment, and the relaxation rate is associated with the muons sensing the background nuclear fields only. At low T of 2.3 K and 5.3 K we had seen at low H_{LF} the muons do not decouple from the local magnetic field environment and there they sense the presence of significant local moments in the muons environment which is different from the background nuclear fields. Furthermore, in this low T regime by going to low H_{LF} value, we see in Fig.6(a)

that there is a drop in the relaxation rate, λ_{fast}^{KT} , as muons sense the frozen glassy magnetic state which sets in the Co₂C NP sample (cf. discussion from the main MS on the glassy state seen below T_{SG} in Fig.1).

Supplementary Information Section IV:

We estimate below the typical size of the regions with short-range order. In order to do this, we determine the average magnetic moment of the cluster regions with short-range order. For doing this, instead of fitting the virgin $M(H)$ curve with a simple Langevin function ($L(\frac{\mu H}{k_B T})$) which implicitly assumes a uniform distribution of magnetic moments (μ), we use the modified Langevin function [5]. The modified Langevin form considers variance in the values of magnetic moments (μ) in the nanocomposite, explicitly a log-normal distribution $f(\mu) = \frac{1}{\mu s \sqrt{2\pi}} \exp(-[\ln(\mu/\xi)]^2/2s^2)$, where s is the variance and ξ is related to the average magnetic moment through, $\mu_{avg} = \xi \sqrt{e^{s^2}}$. The $M(H)$ is fit to the modified Langevin function (as shown in Figure 5 below), viz., $M(H) = N_{cluster} \int_0^\infty \mu f(\mu) L(\frac{\mu H}{k_B T}) d\mu$, where $N_{cluster}$ is a number density parameter. Using $N_{cluster}$, s and ξ as the fitting parameters, we fit the virgin $M(H)$ curve at 2 K using the modified Langevin function; we get $\mu_{avg} = 20 \mu_B$ per cluster of the Co₂C NPs-pellet with $N_{cluster} = 5 \times 10^{19}$ per gram. With magnetic moment per cobalt (Co) atom = $0.066 \mu_B$ at 2 K in Co₂C [1], and there are 6 Co atoms per Co₂C unit cell, one estimates an average size of 50 unit cells per cluster of the region with short-range magnetic order. As each Co₂C unit cell has a volume of 56.65 \AA^3 , and assuming a spherical cluster (island) with short-range

magnetic order, the typical cluster (island) size is $\sim 15 \text{ \AA}$ which is much smaller than a single nanoparticle size of ($\sim 40 \text{ nm}$).

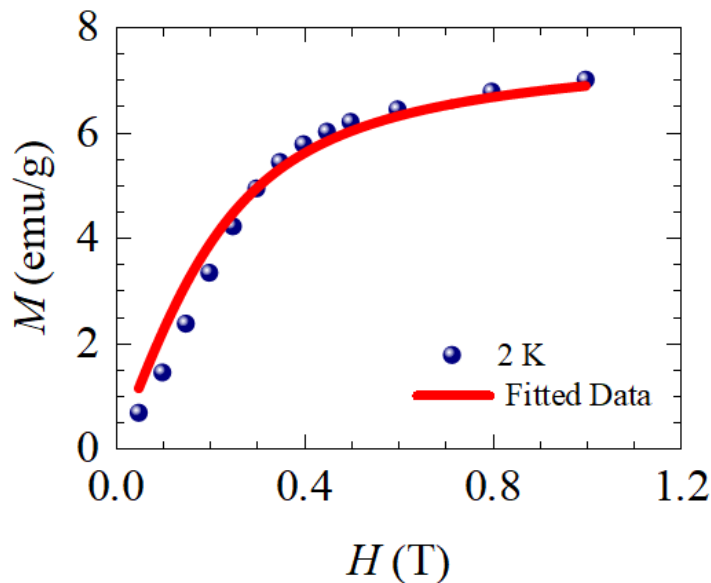


Figure 7. Magnetization versus applied field (M - H) curve at 2 K. The solid red line is the fit to the data with the modified Langevin equation (see text for details).

References:

- [1] Roy N, Ali M A, Sen A, Adroja D T, Sen P and Banerjee S S 2021 Exploring a low temperature glassy state, exchange bias effect, and high magnetic anisotropy in Co_2C nanoparticles *J Phys Condens Matter* **33**
- [2] Yamazaki T 1997 Ryogo Kubo and μSR *Hyperfine Interactions* **104** 3-13
- [3] Larkin M I, Fudamoto Y, Gat I M, Kinkhabwala A, Kojima K M, Luke G M, Merrin J, Nachumi B, Uemura Y J, Azuma M, Saito T and Takano M 2000 Exponential field distribution in $\text{Sr}(\text{Cu}_{1-x}\text{Zn}_x)_2\text{O}_3$ *Physica B: Condensed Matter* **289-290** 153-6
- [4] Biswas P K, Salman Z, Neupert T, Morenzoni E, Pomjakushina E, von Rohr F, Conder K, Balakrishnan G, Hatnean M C, Lees M R, Paul D M, Schilling A, Baines C, Luetkens H, Khasanov R and Amato A 2014 Low-temperature magnetic fluctuations in the Kondo insulator SmB_6 *Physical Review B* **89** 161107
- [5] Silva N J O, Amaral V S and Carlos L D 2005 Relevance of magnetic moment distribution and scaling law methods to study the magnetic behavior of antiferromagnetic nanoparticles: Application to ferritin *Physical Review B* **71** 184408